Received: 30 January 2018 | Accepted: 1 July 2018

DOI: 10.1002/jbio.201800036

Journal of BIOPHOTONICS

FULL ARTICLE

Monte Carlo simulation of polarization-sensitive second-harmonic generation and propagation in biological tissue

K. L. Barry Fung[1]* | Masood Samim[2] | Adam Gribble[3] | Virginijus Barzda[4,5] | I. Alex Vitkin[2,3,6]

[1]Division of Engineering Science, University of Toronto, Toronto, Ontario, Canada

[2]Division of Biophysics and Bioimaging, Princess Margaret Cancer Centre, University Health Network, Toronto, Ontario, Canada

[3]Department of Medical Biophysics, University of Toronto, Ontario, Canada

[4]Department of Chemical and Physical Sciences, University of Toronto Mississauga, Mississauga, Ontario, Canada

[5]Department of Physics, University of Toronto, Toronto, Ontario, Canada

[6]Department of Radiation Oncology, University of Toronto, Toronto, Ontario, Canada

***Correspondence**
K. L. Barry Fung, Division of Engineering Science, University of Toronto, 40 Saint George Street, Toronto, Ontario M5S 2E4, Canada.
Email: king.fung@mail.utoronto.ca

Funding information
Canadian Institutes of Health Research, Grant/Award Numbers: CPG-134752, CHRPJ462842-14; Natural Sciences and Engineering Research Council of Canada, Grant/Award Number: RGPIN-2017-06923

Polarization-sensitive second harmonic generation (p-SHG) is a nonlinear optical microscopy technique that has shown great promise in biomedicine, such as in detecting changes in the collagen ultrastructure of the tumor microenvironment. However, the complex nature of light-tissue interactions and the heterogeneity of biological samples pose challenges in creating an analytical and experimental quantification platform for tissue characterization via p-SHG. We present a Monte Carlo (MC) p-SHG simulation model based on double Stokes-Mueller polarimetry for the investigation of nonlinear light-tissue interaction. The MC model predictions are compared with experimental measurements of second-order nonlinear susceptibility component ratio and degree of polarization (DOP) in rat-tail collagen. The observed trends in the behavior of these parameters as a function of tissue thickness, as well as the overall extent of agreement between MC and experimental results, are discussed. High sensitivities of the susceptibility ratio and DOP are observed for the varying tissue thickness on the incoming fundamental light propagation pathway.

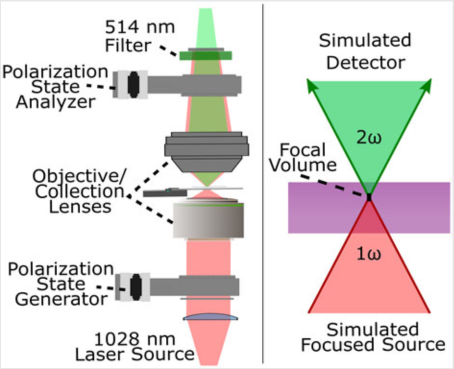

KEYWORDS

light, Monte Carlo method, nonlinear optical microscopy, polarized light microscopy, second harmonic generation microscopy

1 | INTRODUCTION

Second harmonic generation (SHG) microscopy is a noninvasive, label-free technique that is highly sensitive to molecular structure in biological tissue [1–4]. The polarizations of both the incident fundamental photons and outgoing second harmonic photons are known to be important parameters of the SHG process. Specifically, the polarization of outgoing second harmonic photons is dependent on the incident polarization and on the molecular symmetry at the site of SHG. Thus, polarization measurements of SHG, denoted as polarization-sensitive SHG (p-SHG), can be used to obtain information on the organization of tissue [1, 3, 5], through metrics such as the second-order nonlinear optical susceptibility tensor component ratio $|\chi^{(2)}_{zzz}/\chi^{(2)}_{zxx}|$ [6, 7] and the degree of polarization (DOP) of the outgoing light [8, 9]. Recently, p-SHG has been demonstrated to detect previously unresolvable, submicron changes in the extracellular matrix due to tumor progression in thyroid [10], lung [11], and breast tissue [12]. In particular, cancerous tissues were observed to have significant increases in the second-order nonlinear optical susceptibility tensor component ratio $|\chi^{(2)}_{zzz}/\chi^{(2)}_{zxx}|$ compared with healthy tissue. These changes imply that in diseased tissues, SHG intensity generated from incoming light polarized parallel to collagen fibers increased relative to SHG intensity generated from incoming light cross-polarized with the fiber direction. The differences in $|\chi^{(2)}_{zzz}/\chi^{(2)}_{zxx}|$ have been ascribed to growing disorder in the collagen ultrastructure at the submicron level in tumorous tissue [7, 11]. However, while changes in experimentally measured $|\chi^{(2)}_{zzz}/\chi^{(2)}_{zxx}|$ can reflect intrinsic tissue biology including pathological state, they are also undesirably influenced by experimental factors, such as measurement geometry or tissue thickness. Coupled with the inherent spatial heterogeneity of most biological tissue, these factors alter the polarization of light before and after SHG occurs, complicating p-SHG measurements and preventing unequivocal interpretation of results. It would be beneficial to characterize and minimize the effects of these extraneous factors that currently limit quantitative p-SHG analysis to optically thin tissue. We therefore undertake a simulation and experiment-based study of polarization effects in SHG within varying thickness of biological tissues.

Numerical simulations provide a controlled environment for investigation of p-SHG, enabling quantitative predictions of experimental observables otherwise intractable by analytical methods. However, previous efforts to numerically simulate p-SHG did not track polarization of outgoing second harmonic light [13, 14]. Moreover, these simulations neglected scattered light and other stochastic phenomena within turbid and heterogeneous media like biological tissue. As such, they lack applicability to general p-SHG measurements, which utilize input light of nine separate polarizations, and require measuring full polarization information on the outgoing light from SHG. To provide an avenue for studying p-SHG in more complex, highly scattering geometries, we turn toward Monte Carlo (MC) methods.

MC methods have been widely used to characterize laser-tissue interactions and biological response to light [2, 15, 16]. These approaches numerically simulate the photon transport equations by repeated tracking of photon packets and interactions using known microscopic tissue properties; by repeating this process many times (~10^6-10^8 photons), statistically significant accumulated quantities generate predictions for experimental observables. Since the introduction of the method into biomedical optics by Wilson and Adam [17] MC algorithms have been used in linear optics intensity-based biophotonics applications, from determining macroscopic optical properties of heterogeneous tissue [18], to planning and conducting photodynamic therapy for cancer treatment [19]. Some research groups have also reported polarization sensitive extensions of linear MC methods [20–22], including our own model (polMC) [23], which is adapted for the p-SHG work reported here.

Other attempts have previously been made to simulate nonlinear optical processes, such as SHG, via MC methods. LaComb et al implemented a variant of the most prevalent intensity-only (ie, no polarization) package, the MC algorithm for multilayered (MCML) tissue [24], for studying intensity-only SHG [16]. LaComb's algorithm has been applied in combination with experimental imaging to differentiate normal and diseased skin. The algorithm allowed for the characterization of confounding effects due to sample thickness, quantifying the changes in SHG directionality and attenuation between diseased and normal tissues. However, the algorithm neglects the polarization of light, and is thus unsuitable for investigating p-SHG.

In this work, we present a polarization-sensitive MC (Pol-MC) model for simulating SHG and propagation and test its predictions and thus validity by examining focal depth-dependent measurements of $|\chi^{(2)}_{zzz}/\chi^{(2)}_{zxx}|$ and *DOP*. The potential underlying causes of the depth dependencies of $|\chi^{(2)}_{zzz}/\chi^{(2)}_{zxx}|$ and *DOP*, as well as the agreement between measurements and MC predictions, are discussed in the context of previous work in the field, to demonstrate the utility of the model in investigating the complex biophysical environment of biological tissue.

2 | METHODS

The proposed MC algorithm builds on our previously developed and validated Pol-MC model for linear biophotonics applications [23]. Here, we extend the model to simulate nonlinear interactions in tissue (specifically the creation of the second harmonic photons) utilizing the double Stokes-Mueller formalism, while maintaining the ability to account for linear photon interactions at the fundamental (ω) and second harmonic (2ω) frequencies. The simulation models a laser scanning SHG microscope with an incident focusing, polarized light of frequency ω, a turbid sample placed in its path, and a transmission-geometry detector that measures the Stokes vector of resultant 2ω light using polarization state analyzers, replicating the experimental setup described in the following (Figure 1).

2.1 | Experimental setup

The nonlinear Stokes-Mueller polarimetric microscope was described previously [9]. An incident laser beam (power at sample = 21 mW, central wavelength = 1028 nm, pulse repetition frequency = 14.3 MHz) with 400 fs pulses was used [25]. The polarization states were prepared using a computer-controlled polarization state generator (linear polarizer, half-wave plate and quarter-wave plate). The polarized laser beam was propagated upward into an air objective lens with a numerical aperture (NA) of 0.75 (ZEISS Plan-Apochromat 20×, Jena, Germany). The 1028 nm fundamental light focused on a focal volume (with a lateral point spread function of full width at half maximum [FWHM] of 1 μm, and axial FWHM of 3.7 μm) generating second harmonic photons at a selected depth within a sample. The SHG signal was collected at frequency 2ω with a homebuilt 0.85 NA and passed through a computer-controlled polarization state analyzer (quarter-wave

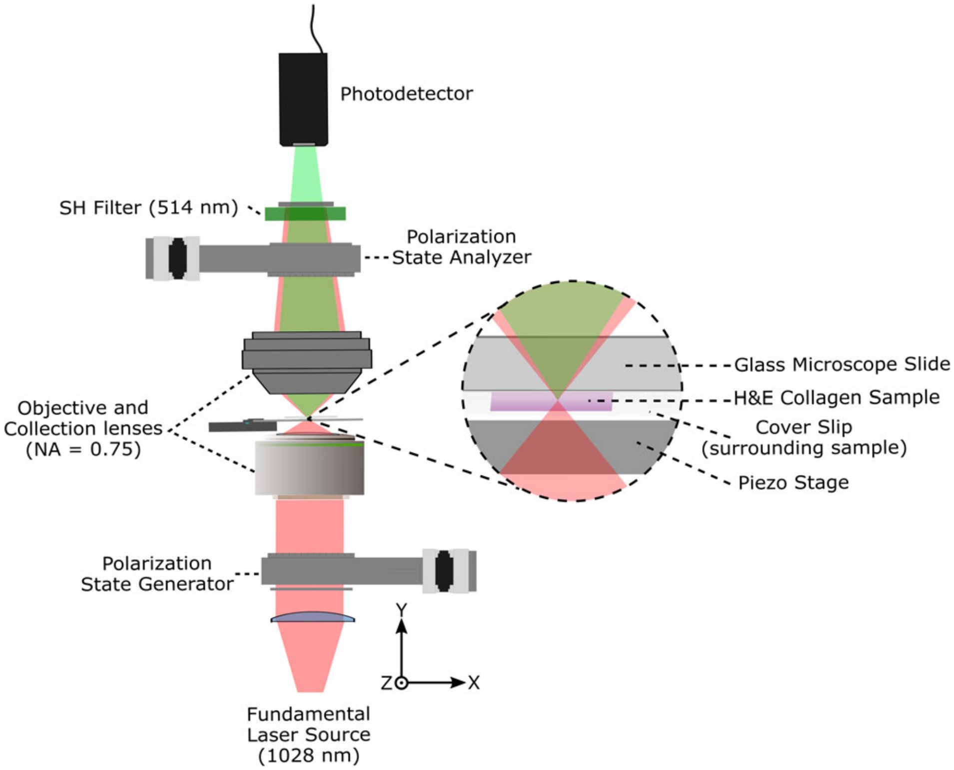

FIGURE 1 The experimental setup, replicated in simulation. The magnified portion shows the sample on a glass microscope slide, placed with cover slip facing toward the source. Red represents the infrared ω light of 1028 nm wavelength, while green represents the second harmonic 2ω light of 514 nm. The axes denote the laboratory reference frame, where Y represents the axis of light propagation and X-Z represents the image plane

plate, half-wave plate and linear polarizer), and filtered through a 510 to 520 nm band-pass filter. This filter blocked any remaining fundamental light, allowing the photodetector (Hamamatsu H7422P-40, Hamamatsu, Japan) to detect only the second harmonic light. Photon counting mode was used for detection with FPGA based data acquisition card (Innovative Integration, X5-210M). An imaging area of 110 × 110 μm^2 was achieved using scanning mirrors (resonant [EOPC SC30, Ridgewood, NewYork] and galvanometric [Cambridge Technology 6220H, Bedford, Massachusetts] mirror pair), yielding a 612 × 612 pixel intensity map of the imaging area for a measurement using a given ω input and 2ω output polarization states.

2.2 | Theory

To simulate p-SHG in optically thick tissue, an MC model was developed. It uses the double Stokes-Mueller formalism for SHG generation in optically thin tissue, as described by Samim et al [1], in tandem with traditional polarization sensitive MC models of light propagation. This formalism describes the polarization of the generated second harmonic light at 2ω frequency as a function of the incident ω polarization and accounts for intrinsic tissue properties as reflected in the nonlinear susceptibilities.

In the double Stokes-Mueller formalism, the outgoing 2ω light is described by the linear Stokes vector $s_{2\omega}$ with parameters $[I, Q, U, V]$, where the lowercase s represents the linear Stokes vector, and the subscript represents the frequency. Specifically, $s_{2\omega}$ is given by:

$$s_{2\omega} = \mathcal{M} S_{\omega} \tag{1}$$

where $\mathcal{M}$ is the double Mueller matrix of the sample as a function of the second-order susceptibility components $\chi^{(2)}$, and S_{ω} is the double Stokes vector of the incoming ω light as a function of its polarization (Stokes vector s_{ω}). The double Mueller matrix is a (4 × 9)-element matrix. It represents the sample's properties for generating 2ω light, and is calculated elementwise [1]:

$$\mathcal{M}_{\gamma N} = \frac{1}{2} Tr\left(\tau_{\gamma} \chi^{(2)} \lambda_{N} \chi^{(2)\dagger}\right) \tag{2}$$

where $\mathcal{M}_{\gamma N}$ is the element of $\mathcal{M}$ in row γ (0-3) and column N (1-9), $Tr()$ represents the trace operation on a matrix, τ_{γ} is the (2 × 2) Pauli matrix of index γ (from 0 to 3), λ_N is the (3 × 3) Gell-Mann matrix of index N (from 1 to 9), $\chi^{(2)}$ is a (2 × 3) matrix of the second-order susceptibility tensor components of the material and † represents the conjugate transpose. Specifically, the Pauli and Gell-Mann matrices relate the electric field of a single photon and the product of the electric field of two photons to the linear Stokes and the double Stokes vectors, respectively [1], and are enumerated in Equation (S1 and S2) in Appendix S1, Supporting Information. On the other hand, $\chi^{(2)}$ represents the generation efficiency for a given set of input and output polarization as denoted by the index of each component. For instance, for $\chi^{(2)}_{aB}$, the element in ath row and Bth column of $\chi^{(2)}$, the first index a represents the axis of the outgoing polarization (typically x and z), while the second index B represents the pair of input polarizations involved in the interaction (typically *xx, zz, xz*). In many cases (including in collagen), materials are assumed to have Kleinman symmetry [26], where the components have interchangeable indices (eg, $\chi^{(2)}_{zxx} = \chi^{(2)}_{xzx} = \chi^{(2)}_{xxz}$), allowing for a simplified analysis.

The double Mueller matrix has several mathematically equivalent forms, each containing the same information concerning the second-order susceptibility $\chi^{(2)}$. One of these is the (6 × 6) susceptibility correlation matrix $X^{(2)}$ [27]:

$$X^{(2)} = \begin{pmatrix} \chi^{(2)}_{1,1}\chi^{(2)*}_{1,1} & \chi^{(2)}_{1,1}\chi^{(2)*}_{1,2} & \cdots & \chi^{(2)}_{1,1}\chi^{(2)*}_{2,3} \\ \chi^{(2)}_{1,2}\chi^{(2)*}_{1,1} & \chi^{(2)}_{1,2}\chi^{(2)*}_{1,2} & & \chi^{(2)}_{1,2}\chi^{(2)*}_{2,3} \\ \vdots & & \ddots & \vdots \\ \chi^{(2)}_{2,3}\chi^{(2)*}_{1,1} & \chi^{(2)}_{2,3}\chi^{(2)*}_{1,2} & \cdots & \chi^{(2)}_{2,3}\chi^{(2)*}_{2,3} \end{pmatrix} \tag{3}$$

where $\chi^{(2)}_{i,j}$ is the *i*th row and *j*th column of $\chi^{(2)}$, the (2 × 3) matrix from Eq. (2). Given the measurement of outgoing 2ω Stokes vectors of a sample for nine different input ω Stokes vectors, the double Mueller matrix is calculated through matrix inversion, while $X^{(2)}$ can be calculated via a robust maximum likelihood estimation (MLE) [27]. Thus, the $X^{(2)}$ representation is preferred for fitting measured input and output Stokes vectors to extract $|\chi^{(2)}_{zzz}/\chi^{(2)}_{zxx}|$, due to the undesirable noise amplification associated with matrix inversion. Conversely, the double Mueller matrix is preferred for calculating outgoing SHG given the incoming Stokes vectors and $|\chi^{(2)}_{zzz}/\chi^{(2)}_{zxx}|$, as there exists no equivalent formulation of the double Stokes-Mueller equation seen in Eq. (1) for $X^{(2)}$. The two matrices are equivalent descriptions of the material and can be converted between each other without change in information. For instance, the element-wise conversion from $X^{(2)}$ to $\mathcal{M}$ is given by:

$$\mathcal{M}_{\gamma N} = \frac{1}{2} Tr\left(\left(\tau_\gamma \otimes \lambda_N^T\right) X^{(2)}\right) \tag{4}$$

where ⊗ is the tensor product operator, and the superscript T represents the matrix transpose operation.

The double Stokes vector S_ω represents the coherent interaction between the incoming photons. For two photons of the same pure (unscattered) polarization, the double Stokes vector can be directly calculated from their linear Stokes vector s_ω using Eq. (5) [1, 28]:

$$S_\omega = \begin{bmatrix} S_1 \\ S_2 \\ S_3 \\ S_4 \\ S_5 \\ S_6 \\ S_7 \\ S_8 \\ S_9 \end{bmatrix} = \begin{bmatrix} \sqrt{\frac{1}{6}}\left(3I_{pol}^2 - Q^2\right) \\ \sqrt{\frac{1}{12}}\left(5Q^2 - 3I_{pol}^2\right) \\ -I_{pol}Q \\ \frac{1}{2}\left(U^2 - V^2\right) \\ U\left(I_{pol} + Q\right) \\ -U\left(Q - I_{pol}\right) \\ -UV \\ V\left(I_{pol} + Q\right) \\ V\left(Q - I_{pol}\right) \end{bmatrix} \tag{5}$$

where Q, U and V are the Stokes parameters for the incoming light s_ω, while $I_{pol} = \sqrt{Q^2 + U^2 + V^2}$ represents the intensity of the fully polarized incoming light. Each of these elements is quadratic with respect to the incoming Stokes vector, indicating the contribution of two photons, and reflect the interaction between their electric fields (eg, the last three elements describe the contribution of circular polarization, and are zero for linearly polarized light).

2.3 | Simulation

The MC algorithm was developed using both the linear propagation methods from Pol-MC and the SHG theory from double Stokes-Mueller formalism. The algorithm is shown in Figure 2, and its two major processes (linear propagation and SHG) are discussed as follows.

Process 1, the linear propagation of polarized light, is performed as in Pol-MC [23]. Photon packets are initialized with a random position within a predefined source, a resultant direction due to focusing, and initial polarization (represented by a Stokes vector s_ω), and are propagated through the biological sample. Samples are modeled as homogeneous tissue layers of average refractive index n_{med}. Tissue anisotropy and resultant birefringence are modeled with an extraordinary refractive index n_{eo} and extraordinary axis $\vec{d}_{eo}$ (the axis along which the altered refractive index is experienced). Scattering in the tissue is modeled as being caused by spheres of radius r_{scat} with refractive index n_{scat}. Photon packets undergo interactions every distance d, where d is sampled from the probability distribution $exp[-\mu_t d]$, where μ_t is the sum of the resultant tissue scattering coefficient μ_s and absorption coefficient μ_a. At each interaction, a fraction of the packet (equal to μ_a/μ_t) is locally absorbed into the medium. The remaining fraction is scattered with a new direction dictated by two angles (φ, θ) randomly sampled from the phase function of each spherical scatterer, where the former determines the rotation of the polarization reference frame, and the latter describes the deflection of the scattered packet from the incoming direction [18]. The scattered packet has its polarization reference frame rotated by φ, such that the axis defining perpendicular polarization is normal to the plane defined by the propagation direction and the new scattered direction (details in Appendix S1, Equations (S3-S12)). This operation redefines the polarization of the packet such that Mie scattering theory is applicable. The packet's polarization is then altered by applying the Mueller matrix parameterized by deflection angle θ, as defined via Mie theory [29].

The photons are thus propagated until: (1) the packet reaches the focal volume, represented by a cylinder centered at the focal point with diameter and height determined by experimental FWHM, (2) the packet intensity drops below a selected threshold (in this work, to $<10^{-99}$ of its initial value) and undergoes standard MCML Russian roulette

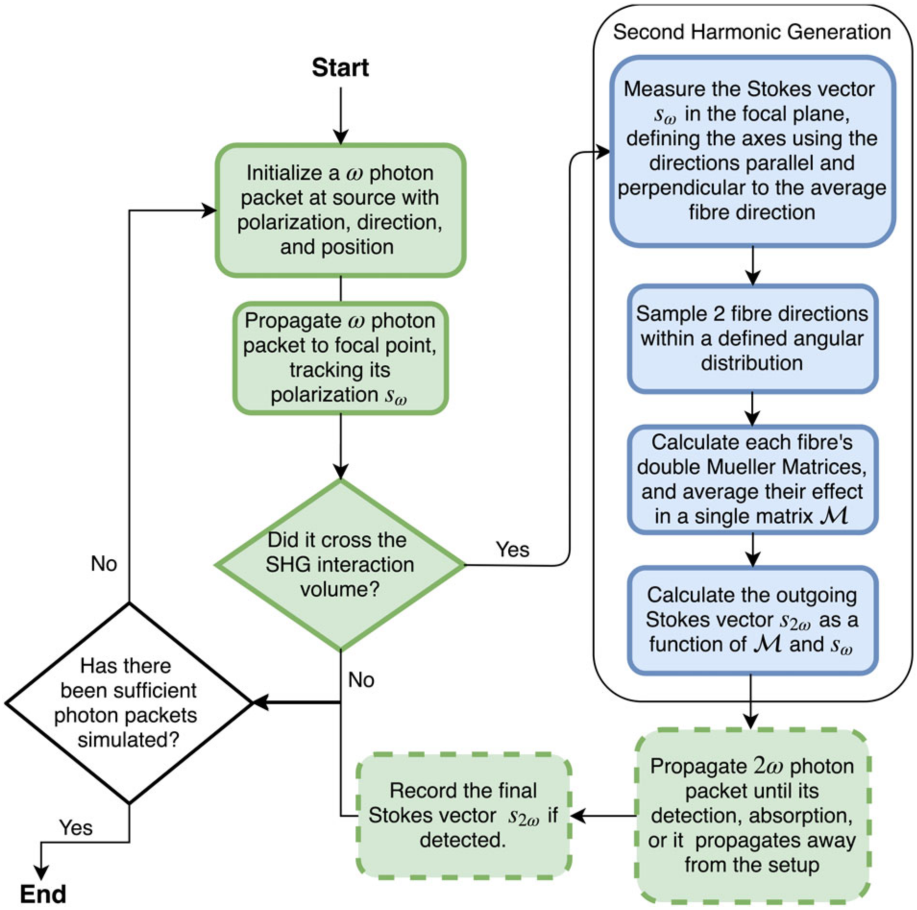

FIGURE 2 General algorithm for the p-SHG MC model. Green boxes represent Process 1 (linear photon propagation: solid outline = ω, hashed = 2ω), while blue boxes represent Process 2 (SHG)

termination [23, 24, 30, 31], (3) the packet propagates away from the sample or (4) hits the detector and filtered out (ie, not recorded) as a representation of the 510 to 520 nm bandpass filter. Changes in polarization during this propagation are tracked using the linear Stokes-Mueller formalism for each interaction (eg, scattering, birefringence). In particular, the Mueller matrix for birefringence is calculated using the angle ϕ between the propagation direction and $\vec{d}_{eo}$, birefringence $\Delta n = \frac{n_o n_e}{\left(n_e^2 \cos^2\phi + n_o^2 \sin^2\phi\right)^{0.5}}$, the distance propagated d, and the wavelength λ [32, 33], while the Mueller matrix for scattering is handled with the Mie theory for spherical scatterers [18, 29].

Process 2, the SHG, employs the double Stokes-Mueller formalism on ω packets modeled through Process 1. As SHG is a coherent process, and MC packets are typically assumed to be incoherent [34], we consider only the set of photons that travel the same path (ie, we draw two photons from the same packet). Due to the quadratic dependence of SHG on the intensity of incoming light [35], 2ω generation is considered to occur only at the focal volume within the sample. Thus, for each incident ω photon packet that crosses the focal volume, a single 2ω packet is generated (terminating the original ω packet) at the center of the focal volume. The propagation direction of the resultant outgoing 2ω photon packet is then set equal to the average direction of the source (along the Y-axis) as an approximation of focusing (discussed as the sixth limitation to the model in the following).

The 2ω polarization is calculated using the Stokes vector s_ω of the incident photon at the focal volume, as well as the second-order susceptibility components $\chi^{(2)}$ of the material, using the formalism described in Section 2.2 [1]. The Stokes vector s_ω is calculated by measuring the polarization of the packet in the plane of the fibers, using the formalisms described by Côte and Vitkin [23] and Jaillon et al. [29]. Its reference frame is specified by the average collagen fiber orientation (assumed to be along the extraordinary axis $\vec{d}_{eo}$), as well as the vector $(\vec{d}_{eo} \times \hat{y})$, yielding the parallel and perpendicular polarization axes (z and x, respectively) with respect to the detection plane. $\chi^{(2)}$ is derived experimentally from measurements of optically thin samples (approximately equal to molecular $\chi^{(2)}$ as there are minimal tissue scattering effects) and used as an input simulation in the form of $\left|\chi^{(2)}_{zzz}/\chi^{(2)}_{zxx}\right|_{mol}$, the molecular susceptibility ratio of the collagen fiber at the site of generation. For cylindrically symmetric molecules with Kleinman symmetry such as collagen and myosin, this ratio defines the more important components of $\chi^{(2)}$ [1]. In addition, the effect of multiple fibers is accounted for; this is important as multiple fibers or fibrils within the interaction volume can contribute to the process. As a first approximation, we consider two fibers for each generated photon, calculate the double Mueller matrix associated with each fiber, and average the two. Specifically, the double Mueller matrices are calculated from the susceptibility of collagen fibrils at angles selected from a von Mises angle distribution centered at the bulk angle of the collagen fiber orientation, along the extraordinary axis $\vec{d}_{eo}$, providing the simplest model of fiber direction heterogeneity in the interaction volume. The von Mises distribution is described by an experimentally determined shape parameter K which governs the width of the angular fiber orientation spread [36], where higher K values result in narrower angular distributions.

With these polarization ($s_{2\omega}$) and direction parameters determined, the 2ω packets then propagate in a similar manner to the fundamental ω photon packets (Process 1), with optical properties at the new halved wavelength. The packet is tracked until it exits the sample and is detected, its intensity drops below the previously mentioned threshold, or it propagates away from the set up.

There are some assumptions within the proposed p-SHG simulation platform. (1) Each photon packet interacts only with the medium, but not with other photon packets, following the assumption that the vast majority of photon packets in MC simulations are incoherent with each other [34] and are thus unusual for a coherent process. The simulation thus considers only photon pairs of identical polarization (ie, photons in the same packet) during SHG. (2) Due to the quadratic dependence of SHG, the focal volume is assumed to be the only location where SHG occurs. The bulk of SHG is indeed known to occur in the focal volume [35, 37] and equivalent assumptions appear in other MC models of SHG [16], so this assumption is unlikely to be too restrictive. (3) The fibrous tissue is modeled as a suspension of spherical scatterers; to compensate for this simplification, bulk optical parameters (n_{med}, $n_{eo} = n_{\text{med}} + \Delta n$, n_{scat}, μ_s and μ_a) are included [23]. Previous Pol-MC studies have demonstrated that the polarization properties of tissue can indeed be modeled accurately as one or more turbid layers with average bulk properties [23, 32, 38]. However, there are some differences between the geometry of the modeled spherical scatterers and the actual cylindrically shaped fibers common to collagen. For example, the former has a much simpler Mie scattering solution compared to the latter, and its phase function is independent of photon direction due to the scatterer's spherical symmetry; conversely scattering from a cylinder depends on the photon's incident angle with respect to the scatterer axis. However, for the incidence angular ranges used in this study ($\theta < 45°$, corresponding to NA = 0.7), both spherical and cylindrical have largely forward scattering phase functions, mitigating the effects of this particular simplification [39]. That said, future modeling efforts will focus on incorporating the more complex and computationally expensive cylindrical scatterer formalism. (4) The model currently uses two fibers to simulate the effect heterogeneous directional orientation of multiple fibers within an interaction volume. While possible to incorporate the contributions of more fibers, decomposition of the Mueller matrix and its mathematical equivalents indicate that the effect of more than two fibers can be expressed as a combination of two fibers [Krouglov and Barzda, (2017), unpublished data]. For this work, we begin with the simpler two-fiber formulation as a basic model of multifiber disorder, with investigations into more fiber refinements planned for the future. (5) The model currently assumes that incident polarization states lie entirely within the image plane, thus neglecting any polarization that may occur along the average propagation direction (Y-axis in Figure 1). This underestimates of the amount of resulting SHG, as this polarization that is neglected should still contribute to the outgoing photon. This effect also increases with maximal half angle of the incident photon with respect to the average propagation direction. The model is thus more accurate at lower NA arrangements and may underestimate the contribution of high-incident-angle (and likely highly scattered) photons. (6) The direction of the SHG photon packet emanating from the focal volume is along the principal axis of the source (the Y-axis in Figure 1). This simplification results in a uniform effect by the post-SHG thickness of samples for all light in the sample. The simulation thus removes the contribution of SHG emission geometry to outgoing polarization when compared to the experimental setup. However, the use of a photomultiplier (ie, a single element detector) already averages over the entire emission geometry, making the effects of this simplification minimal. Further extensions to the model may account for the emission patterns of SHG [4, 40, 41] to validate the effects of this assumption.

2.4 | Validation methods

To validate the MC model, p-SHG measurements were performed on rat-tail collagen of varying thicknesses (either with increasing thickness before or after SHG) utilizing the setup in Figure 1 and compared to corresponding MC simulation predictions. Experimental validation studied the effects of thickness on $|\chi^{(2)}_{zzz}/\chi^{(2)}_{zxx}|$ and DOP; note that as the values of both quantities of the thinnest sample (~6 μm) were input into the simulation, the validation focused on the trend of each observable as a function of thickness, as commonly done when comparing normalized data.

2.4.1 | Samples

Rat-tail tendon was chosen due to the purity of its composition (almost 100% collagen), and the strong alignment of its fibers. Each rat-tail tendon sample was fixed, paraffin embedded and cut axially (along the fibril alignment direction) into thin sections of increasing thickness (~5, 10, 20, 30 and 40 μm). Sections were stained with hematoxylin and eosin (H&E) and mounted on a glass slide with a cover slip. It should be noted that formalin fixation changes tissue polarization properties slightly [42], but the relative data trends as examined here are likely unaffected. Similarly, H&E staining changes the absorption profile of collagen, with increases in absorption in the visible light spectra [43]; these increases may be present to varying modest extents at our 1028 and 514 nm wavelengths of interest and may cause an overall slight decrease in light intensity (due to absorption) and a slight increase in DOP (as highly scattered [depolarized] photons are more likely to be absorbed). However, H&E staining was necessary for identification of regions of interest (ROI) with aligned, parallel collagen fibers using bright field microscopy. Each of the experiments measuring $|\chi^{(2)}_{zzz}/\chi^{(2)}_{zxx}|$ or *DOP* with increasing ω or 2ω thickness was carried out on slices from the same tendon. To minimize intersampling variability, the ROIs from adjacent samples (eg, the 5 and 10 μm samples, the 10 and 15 μm samples, and so on) were chosen such that they were contiguous in the original tendon before sectioning. Detailed sample information for each experiment is included in Table S1 in Appendix S1.

2.4.2 | Measurement procedure

Each collagen sample was placed on the piezo stage and with its cover slip facing downward toward the laser light source. The samples were oriented such that their fibers had the same orientation in the X-Z plane (Figure 1) of the laboratory frame of reference across all thicknesses. This allowed us to assess the effects of consistent sample anisotropy (eg, birefringence) on measured values.

For each sample, double Stokes-Mueller polarimetry measurements were performed on a 110 × 110 μm^2 region to characterize the double Mueller matrix for each of the 612 × 612 pixels (size ~0.18 × 0.18 μm^2) of the tissue. Each measurement consisted of six intensity-based analyzer measurements (counting the number of photons over 20 seconds) of outgoing Stokes vector $s_{2\omega}$ for nine input double Stokes states S_ω as defined by Samim et al [1] (Equation S3 in Appendix S1). These measurements allow for the MLE of the susceptibility correlation matrix $X^{(2)}$.The decomposition of the $X^{(2)}$ matrix, as well as examinations of the outgoing Stokes vector for each experiment, yields a map of: (1) the ratio $|\chi^{(2)}_{zzz}/\chi^{(2)}_{zxx}|$, (2) the *DOP* and (3) the sample orientation angle δ with respect to laboratory Z-axis. The first two parameters are suitable for validating comparisons with the MC simulations, while the third parameter describes the orientation of the collagen fiber within the image plane (perpendicular to the direction of propagation) in radians from the Z-axis in the laboratory frame of reference and is used in simulation afterward.

TABLE 1 Wavelength-dependent tissue properties used in the simulation. The refractive indices specified are for the ordinary axis of the sample (n_{med}), the extraordinary axis of the sample (n_{eo}), and the scatterers (n_{scat}). The scattering and absorption coefficients are specified by μ_s and μ_a, respectively

Wavelength [nm]	n_{med} [44]	n_{eo} [45]	n_{scat} [46]	μ_s [cm^{-1}][47]	μ_a [cm^{-1}][47]
1028	1.345	1.348	1.46	150	0.3
514	1.348	1.351	1.50	300	1.3

In each experiment, collagen samples of increasing thickness (Table S1 in Appendix S1) were placed such that the focal volume was situated at the selected depth. The thickness of each sample's selected ROI was measured by vertically adjusting the piezo stage and evaluating the intensity of SHG at each position. By recording the stage positions where SHG began to occur and where it ceased, the location of the surfaces of the tissue were measured, yielding the sample thickness. The piezo stage was then adjusted to position the focus at the correct preselected sample depth for each experiment. In the first set of experiments, the focal depth was fixed such that there was 2 μm of tissue after SHG. The thickness of the tissue before SHG (affecting ω photons) was then varied. In the second set of experiments, the focal depth was fixed such that there was 3 μm of tissue before SHG, and the thickness of the tissue after SHG (affecting 2ω photons) was varied.

2.4.3 | Simulation procedure

The measurements of collagen samples as a function of thickness before and after SHG were also repeated using the simulation algorithm as defined in Figure 2, modeling collagen as a spherical scatterer of radius 0.9 μm, with the wavelength-dependent parameters in Table 1.

For the purposes of simulation, the molecular susceptibility ratio $|\chi^{(2)}_{zzz}/\chi^{(2)}_{zxx}|_{\text{mol}}$ of collagen was presumed to be equivalent to that of the thinnest sample in each simulation (~5-8 μm), and assumed to be real, with no phase. This is a reasonable assumption, since minimal tissue is involved before and after SHG in thin samples, allowing the measurement to closely approximate the molecular value [12]. Similarly, the von Mises shape parameter K of the fibril distribution was chosen such that the simulated *DOP* of the SHG signal of the thinnest sample approximately equalled the DOP in experimental measurements. The input was solved for iteratively in simulation, varying K until an appropriate DOP was achieved for the thinnest sample. Resultant K values were ~132 and ~250 for the first and second experiments, respectively, yielding corresponding von Mises distributions with standard deviations (SDs) of 5° and 3.8° (differences may be due to ROI selection).

As mentioned before, the absolute magnitudes of the measured $|\chi^{(2)}_{zzz}/\chi^{(2)}_{zxx}|$ and *DOP* cannot be used for validation, because the value of these parameters for the thinnest sample serve as inputs to the simulation. However, trends in $|\chi^{(2)}_{zzz}/\chi^{(2)}_{zxx}|$ and *DOP* as a function of tissue thickness can serve this purpose.

The SHG laser scanning microscopy setup was replicated in simulations, where the light was focused with an NA of 0.7 onto a sample and a transmission-geometry detector measured the detected second harmonic light. The sample orientation in the image plane was chosen such that the collagen fiber angle in the image plane was equal to the angle δ from the Z-axis calculated from the experimental analysis of the $|\chi^{(2)}_{zzz}/\chi^{(2)}_{zxx}|$ and from examination of SHG intensity images. Each simulation, corresponding to a given experiment, was repeated 25 times with a minimum of 4.5×10^5 photons. As MC simulation noise scales with $1/\sqrt{N}$, where N is the number of photons, this threshold of 10^7 photons per simulation minimizes noise within reasonable run times (1-2 hours for thinner samples, ~30 hours for thicker samples on an Intel Core i5-4460 with 8 GB of RAM).

2.5 | Signal processing

Recorded data were processed by a combination of custom software written in LabView (National Instruments, Austin, Texas), MATLAB (MathWorks, Natick, Massachusetts) and C++ to produce six intensity images (612 × 612), and was visualized using MATLAB, NumPy [48] and Matplotlib [49]. Experimental results were first binned in 4 × 4 pixel groups to provide sufficient signal for analysis. Specifically, the 16 pixels were replaced with a single large pixel of equal total area (~$0.72 \times 0.72\ \mu m^2$) containing the sum of the intensity detected in the 16 smaller pixels. Within the resulting image of 153 × 153 large pixels, the image was cropped to minimize effects due to nonideal mirror movement, and remaining pixels that still had intensities below a preselected threshold were discarded and ignored in further analysis, preventing unwanted artifacts.

For each remaining large pixel in each measurement, and for each measurement in simulation, the outgoing Stokes vector was calculated for each of the nine incoming Stokes vectors (Equation S13 in Appendix S1). These nine sets of outgoing and incoming Stokes vectors provide sufficient information for the MLE of the correlation matrix $X^{(2)}$ for each pixel, as presented in by Samim et al. [27]. Specifically, the Cholesky decomposition of $X^{(2)}$ is used to calculate the theoretical outgoing Stokes vector, given the input states of polarization, as seen in equation 17 from Ref. [27]. Minimizing the difference between the theoretical outgoing Stokes vector with the measured Stokes vector with respect to $X^{(2)}$ using equation 18 from Ref. [27] yields the MLE as desired. The parameter $|\chi^{(2)}_{zzz}/\chi^{(2)}_{zxx}|$ and sample orientation angle δ with respect to Z-axis can then be calculated as a nonlinear fit to $X^{(2)}$ using its definition in Equation (3). This yielded a map of measured $|\chi^{(2)}_{zzz}/\chi^{(2)}_{zxx}|$ and δ for each experiment and corresponding simulation. Finally, the orientation angle was visually compared with SHG intensity scans and verified to be within estimated upper and lower bounds, lending credence to the analysis.

In determining the DOP as a function of thickness, the outgoing Stokes vector was calculated only for the incoming linear Stokes vector that was closest in angle to the axis of the collagen fiber determined by the average sample orientation angle from the $X^{(2)}$ matrix analysis. This produced the largest signal for the outgoing second harmonic light and maximized the signals to noise ratio, allowing for more robust calculations. [12] The DOP was calculated for each pixel using its definition:

$$\mathrm{DOP} = \sqrt{Q^2 + U^2 + V^2}/I \qquad (6)$$

The mean and SD for both $|\chi^{(2)}_{zzz}/\chi^{(2)}_{zxx}|$ and DOP were then calculated across all analyzed pixels in each sample, yielding a bulk value for each sample thickness.

3 | RESULTS AND DISCUSSION

The experimental results and corresponding simulations trends demonstrating the effects of sample thickness on ratio and DOP before and after SHG are shown in Figures 3 and 4, respectively. The thickness t for each graph is given as the total thickness minus the fixed offset for each experiment. All experimental data represent the mean and SD of $n > 100$ bins for each thickness (with variations due to thresholding), while each corresponding MC model prediction represents the mean and SD of $n = 25$ simulation runs. Error bars represent one SD from the mean, though some simulation results have error values too small to visualize.

In the first set of experiments, the thickness before SHG (affecting ω light) was varied, while the thickness after SHG was kept constant at 2 μm. For each thickness, both $|\chi^{(2)}_{zzz}/\chi^{(2)}_{zxx}|$ and *DOP* were measured, yielding the results in Figure 3. Note the agreement in Figures 3A and 3B, where both measured parameters decrease as a function of thickness.

In the second set of experiments, the thickness after SHG (affecting 2ω light) was varied, while the thickness before SHG was kept constant at 3 μm. For each thickness, both $|\chi^{(2)}_{zzz}/\chi^{(2)}_{zxx}|$ and *DOP* were measured, yielding the results in Figure 4. Note the agreement within one SD for each measurement in Figures 4A and 4B, where $|\chi^{(2)}_{zzz}/\chi^{(2)}_{zxx}|$ appears to have minor decreases as a function of thickness, while the *DOP* stays constant over the examined thicknesses ranges.

The encouraging general agreement between simulation and experiment gives credence to the developed p-SHG MC model, indicating that its overall formulation is correct, and robust prediction of tissue thickness-dependent p-SHG

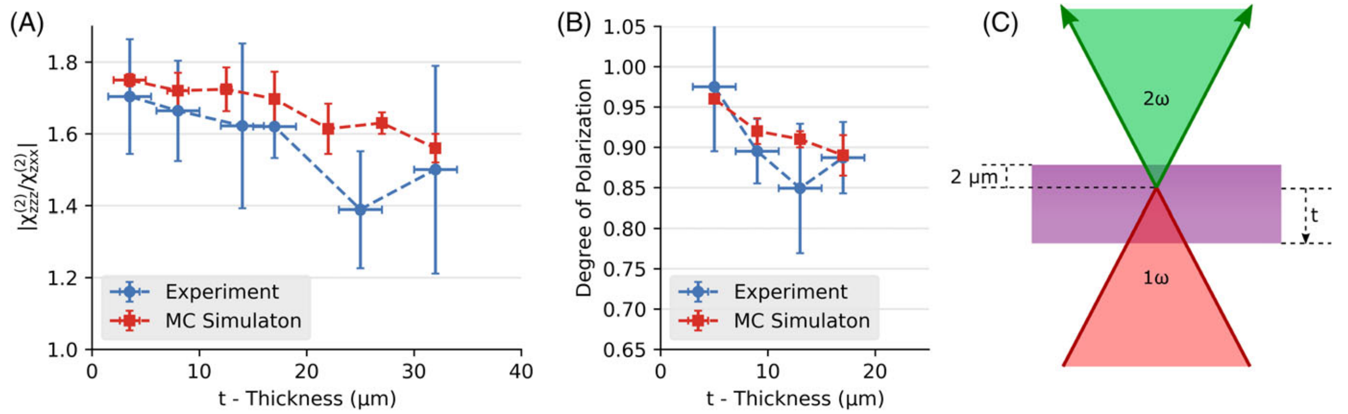

FIGURE 3 Experimental and simulated (A) $|\chi^{(2)}_{zzz}/\chi^{(2)}_{zxx}|$ and (B) *DOP* vs sample thickness, with increasing thickness before SHG; (C) the set up was fixed such that focal depth was fixed at 2 μm below the surface of the tissue near the detector. $|\chi^{(2)}_{zzz}/\chi^{(2)}_{zxx}|$ measurements were performed twice over varying thickness ranges, and were averaged between samples of similar thicknesses, with the first three experimental points and first four simulated predictions representing averages corresponding to the two experimental runs. DOP measurements were performed once over a smaller thickness range, due to the initial experimental run having inconsistent sample anisotropy directions. The points represent experimental ($n > 100$) and simulated ($n \geq 25$) data, while the lines are a guide for the eyes. Error bars represent one SD from the mean and are too small to visualize in some simulations. Note the general agreement of $|\chi^{(2)}_{zzz}/\chi^{(2)}_{zxx}|$ and DOP trends between theory and experiment, with both decreasing as a function of thickness, though there is more uncertainty in experimental results

experimental observables may be possible. We discuss a few important observations in the following.

First, we discuss the usage of the simulation inputs $|\chi^{(2)}_{zzz}/\chi^{(2)}_{zxx}|_{mol}$ and *K,* noting the resultant values of their affected experimental measurements ($|\chi^{(2)}_{zzz}/\chi^{(2)}_{zxx}|$ and DOP, respectively). In the first set of simulations involving thickness before SHG (Figure 3), good agreement is observed in the simulated and experimental value of measured $|\chi^{(2)}_{zzz}/\chi^{(2)}_{zxx}|$ (Figure 3A) and for the value of *DOP* (Figure 3B) for the thinnest sample. There are small differences in the initial values in the simulation and experimental measurements of the ratio and DOP for variation of outgoing tissue thickness (see Figures 4A and 4B). Small discrepancies in the initial values of both parameters are accepted, as they are within the error margins of the measurements.

Second, we discuss the general trends revealed in Figures 3 and 4. Figure 3 shows the decreasing trends in measured $|\chi^{(2)}_{zzz}/\chi^{(2)}_{zxx}|$ (Figure 3A) and DOP (Figure 3B) as a function of thickness affecting fundamental light path length through the tissue. The trends in both Figure 3A, and 3B demonstrate agreement in simulation and measurement. The observed depth dependence of $|\chi^{(2)}_{zzz}/\chi^{(2)}_{zxx}|$ in Figure 3A likely stems from scattering. As optical thickness increases before SHG, the incident ω light on a particular collagen fiber within the focal volume becomes less polarized, eventually resulting in the probing of collagen with unpolarized light [50]. This causes the susceptibility component ratio $|\chi^{(2)}_{zzz}/\chi^{(2)}_{zxx}|$ to tend toward unity–as thickness increases, both light that is initially parallel or perpendicular to the fiber will be increasingly depolarized upon arrival at the focal volume, making the generated light for all inputs effectively equal (ie, the apparent $\chi^{(2)}_{zzz}$ and $\chi^{(2)}_{zxx}$ are equal and $|\chi^{(2)}_{zzz}/\chi^{(2)}_{zxx}|$ is ~1). The underlying trend for Figure 3B, a decreasing DOP with increasing tissue thickness before focal

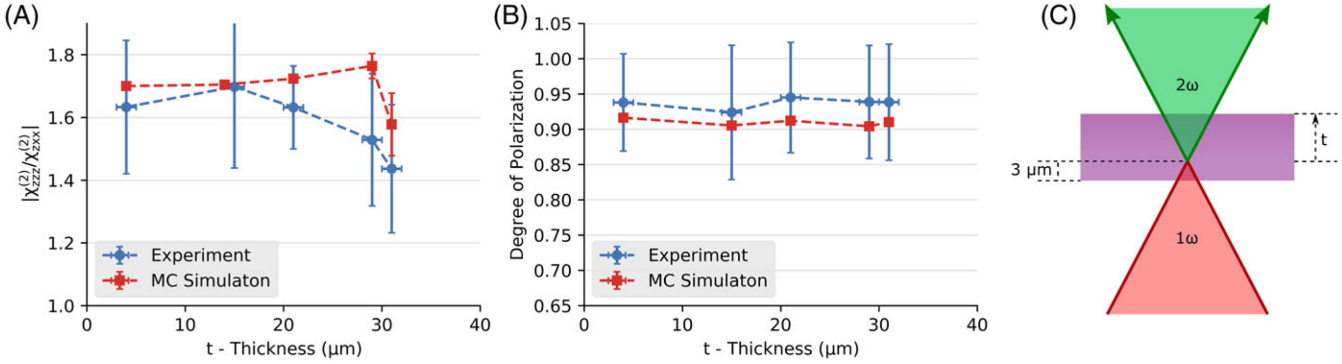

FIGURE 4 Experimental and simulated (A) $|\chi^{(2)}_{zzz}/\chi^{(2)}_{zxx}|$ and (B) DOP vs sample thickness, with increasing thickness after SHG; (C) the set up was fixed such that focal depth was fixed at 3 μm from the surface of the tissue near the source. The points represent experimental ($n > 100$) and simulated ($n = 25$) data, while the lines are a guide for the eyes. Note the agreement in theoretical and experimental trends of the $|\chi^{(2)}_{zzz}/\chi^{(2)}_{zxx}|$ as a function of the thickness, and the interesting result that thickness has negligible effect on DOP, reinforced by the small uncertainty in simulation. A slight variation in the $|\chi^{(2)}_{zzz}/\chi^{(2)}_{zxx}|$ between simulation and experiment is also observed

volume, is also thought to be due to scattering effects, compounded by the nonlinear dependence of SHG on the incident polarization. When ω light scatters, it not only depolarizes, but also changes its polarization as a function of the scattered angle. While the variations in the polarization of ω light caused by scattering are typically small, the quadratic relationship between the incident polarization and the outgoing second harmonic polarization (Equation (5)) further amplify any variation from the initial polarized state. While each generated outgoing 2ω photon packet is fully polarized, the average incident light becomes less polarized as the number of possible states increases with increasing sample thickness, yielding the trends shown in Figure 3B.

The $|\chi^{(2)}_{zzz}/\chi^{(2)}_{zxx}|$ findings are comparable with those of Gusachenko et al [13], who examined depth dependence for a single, optically thick collagen fiber sample. They noted similarly decreasing susceptibility ratios, which were analyzed by comparing the total intensity generated by incident linear polarization aligned parallel to and perpendicular to the collagen fibers. The authors also report large changes in $|\chi^{(2)}_{zzz}/\chi^{(2)}_{zxx}|$ due to the diattenuation effect; this effect is included in as part of our p-SHG MC implementation but was not accounted for explicitly in the simulations reported here. This may contribute to the slightly steeper slope in the experimental measurements of $|\chi^{(2)}_{zzz}/\chi^{(2)}_{zxx}|$ as a function of ω tissue thickness to MC predictions. The influence of this diattenuation effect will be investigated in the future.

Figure 4A shows the trends in the $|\chi^{(2)}_{zzz}/\chi^{(2)}_{zxx}|$, and Figure 4B shows the DOP as a function of tissue thickness after SHG (ie, with increasing sample thickness for 2ω photons). The trends with thickness show agreement between experiment and simulation for both $|\chi^{(2)}_{zzz}/\chi^{(2)}_{zxx}|$ and DOP. The ratio $|\chi^{(2)}_{zzz}/\chi^{(2)}_{zxx}|$ after SHG (Figure 4A) appears to stay initially constant with the increase of 2ω-photon traveling path length and begins to decrease beyond a certain thickness threshold. The initial constancy is thought to be due to the definition of $|\chi^{(2)}_{zzz}/\chi^{(2)}_{zxx}|$–both components in the ratio result in polarized 2ω light parallel to the focal volume symmetry axis. As such, the effect of the tissue applies evenly to both polarization states, keeping the ratio relatively unaffected. Thus, the changes due to birefringence and scattering are unlikely to affect $|\chi^{(2)}_{zzz}/\chi^{(2)}_{zxx}|$ for smaller optical thicknesses. However, as thickness increases, the probability of scattering and absorption increases, broadening the range of output intensities and polarizations, resulting in a more uncertain measurement of $|\chi^{(2)}_{zzz}/\chi^{(2)}_{zxx}|$. The general decrease in the susceptibility ratio observed experimentally may also be due to diattenuation. The assumption of Kleinman symmetry [1, 26] for analyzing the susceptibility of collagen presumes that $\chi^{(2)}_{zxx}=\chi^{(2)}_{xzx}=\chi^{(2)}_{xxz}$. Collagen, however, has lower transmission along its fiber axis due to its absorption. Thus, while $\chi^{(2)}_{zzz}$ and $\chi^{(2)}_{zxx}$ attenuate equally, $\chi^{(2)}_{xzx}$ with its outgoing SH polarization perpendicular to the fiber axis will attenuate less. Thus, estimation of the $X^{(2)}$ matrix under Kleinman symmetry assumption could overestimate $\chi^{(2)}_{zxx}$ and lower the apparent ratio.

Figure 4B shows no significant change in DOP as a function of thickness SHG. This is surprising, as increased thickness is typically associated with increased scattering and thus depolarization (eg, Figure 3B). A plausible explanation for the negligible DOP change may stem from two reasons. First, while there should be a decrease in DOP due to polarization changes via scattering, these polarization changes due to increase in thicknesses may not show observable effects at these optical thicknesses. In comparison with the experiments increasing thickness before SHG (as shown in Figure 3B), these small variations in light do not undergo nonlinear processes, keeping them unamplified. Second, the decreased albedo and increased absorption due to H&E staining [44] at the second harmonic wavelength may cause more highly scattering photons to be preferentially absorbed. As the absorption of the medium increases, the light that undergoes more scattering is less likely to be detected, due to its longer path length. While previous studies have reported that H&E has had minimal effect on SHG [51] and third harmonic generation [52], these studies were done with optically thin (3-5 μm) tissue. The effects inherent in thick tissue were thus not present, as they are in our reported study. The H&E staining effect could also explain the findings of Nadiarnykh and Campagnola [50], who observed significant decreases in DOP of linearly propagated light (900 nm) as a function of thickness. Their study utilized unstained collagen, which allows for more scattering and depolarization given the lower absorption.

4 | CONCLUSION

This work presents an MC simulation model for p-SHG in thick biological tissues. Initial experimental validation in fixed, stained collagen samples revealed similar trends to those predicted by simulations, as a function of both pre- and post-SHG tissue thickness. This gives credence to the validity of the proposed MC model. The effects of other simplifying model assumptions will be pursued in follow-up studies. We envision utilizing the MC simulation on complex tissues and performing sensitivity analyses for the p-SHG technique, most notably to determine the value of $|\chi^{(2)}_{zzz}/\chi^{(2)}_{zxx}|$ independent of extraneous sample and/or experimental geometry parameters. Further MC usage may include investigation of the effects of tissue entropy [53], tissue heterogeneity along the axis of propagation, as well the effects of different measurement setups, such as endoscopy, on the determination of the $|\chi^{(2)}_{zzz}/\chi^{(2)}_{zxx}|$ metric, thus improving the robustness of p-SHG for evaluating tissue organization and pathology.

ACKNOWLEDGMENTS

The authors would like to thank Dr Margarete K. Akens (University of Toronto) and Dr Carl Fisher (University of Toronto) for their assistance in obtaining biological samples and Dr Lukas Kontenis (University of Toronto) for their technical support with the microscopy experiments. This work was supported by Natural Sciences and Engineering Research Council of Canada and the Canadian Institutes of Health Research grants (RGPIN-2017-06923, CPG-134752 and CHRPJ462842-14).

Author contributions

B.F. developed and implemented the model, carried out the validating experiments and prepared the manuscript. M.S. provided input for the double Mueller-Stokes algorithm, and helped to carry out the experiments. A.G., V.B. and A.V. conceived the study, oversaw the model development and experiments, and provided scientific guidance throughout. All authors wrote, edited and reviewed the manuscript.

AUTHOR BIOGRAPHIES

Please see Supporting Information online.

ORCID

K. L. Barry Fung http://orcid.org/0000-0002-7925-8033

REFERENCES

[1] M. Samim, S. Krouglov, V. Barzda, *J. Opt. Soc. Am. B* **2015**, *32*, 451.
[2] F. S. Pavone, P. J. Campagnola, *Second Harmonic Generation Imaging*, CRC Press, Boca Raton **2016**, p. 3.
[3] M. Strupler, A. M. Pena, M. Hernest, P. L. Tharaux, J. L. Martin, E. Beaurepaire, M. C. Schanne-Klein, *Opt. Express* **2007**, *15*, 4054.
[4] L. Moreaux, O. Sandre, J. Mertz, *J. Opt. Soc. Am. B* **2000**, *17*, 1685.
[5] S. W. Chu, S. Y. Chen, G. W. Chern, T. H. Tsai, Y. C. Chen, B. L. Lin, C. K. Sun, *Biophys. J.* **2004**, *86*, 3914.
[6] A. E. Tuer, S. Krouglov, N. Prent, R. Cisek, D. Sandkuijl, K. Yasufuku, B. C. Wilson, V. Barzda, *J. Phys. Chem. B* **2011**, *115*, 12769.
[7] A. E. Tuer, M. K. Akens, S. Krouglov, D. Sandkuijl, B. C. Wilson, C. M. Whyne, V. Barzda, *Biophys. J.* **2012**, *103*, 2093.
[8] N. Mazumder, C.-W. Hu, J. Qiu, M. R. Foreman, C. M. Romero, P. Török, F. J. Kao, *Methods* **2013**, *66*, 237.
[9] L. Kontenis, M. Samim, A. Karunendiran, S. Krouglov, B. Stewart, V. Barzda, *Biomed. Opt. Express* **2016**, *7*, 559.
[10] D. Tokarz, R. Cisek, A. Golaraei, S. L. Asa, V. Barzda, B. C. Wilson, *Biomed. Opt. Express* **2015**, *6*, 3475.
[11] A. Golaraei, R. Cisek, S. Krouglov, R. Navab, C. Niu, S. Sakashita, K. Yasufuku, M. S. Tsao, B. C. Wilson, V. Barzda, *Biomed. Opt. Express* **2014**, *5*, 3562.
[12] A. Golaraei, L. Kontenis, R. Cisek, D. Tokarz, S. J. Done, B. C. Wilson, V. Barzda, *Biomed. Opt. Express* **2016**, *7*, 4054.
[13] I. Gusachenko, M. C. Schanne-Klein, *Phys. Rev. A* **2013**, *88*, 053811-1.
[14] I. Gusachenko, G. Latour, M.-C. Schanne-Klein, *Opt. Express* **2010**, *18*, 19339.
[15] C. Zhu, Q. Liu, *J. Biomed. Opt.* **2013**, *18*, 50902.
[16] R. LaComb, O. Nadiarnykh, P. J. Campagnola, *Biophys. J.* **2008**, *94*, 4504.
[17] B. C. Wilson, G. Adam, *Med. Phys.* **1983**, *10*, 824.
[18] M. Friebel, A. Roggan, G. Müller, M. Meinke, *J. Biomed. Opt.* **2006**, *11*, 34021.
[19] O. Barajas, Å. M. Ballangrud, G. G. Miller, R. B. Moore, J. Tulip, *Phys. Med. Biol.* **1997**, *42*, 1675.
[20] S. Bartel, A. H. Hielscher, *Appl. Optics* **2000**, *39*, 1580.
[21] M. J. Raković, G. W. Kattawar, M. B. Mehrubeoğlu, B. D. Cameron, L. V. Wang, S. Rastegar, G. L. Coté, *Appl. Optics* **1999**, *38*, 3399.
[22] J. C. Ramella-Roman, S. A. Prahl, S. L. Jacques, *Opt. Express* **2005**, *13*, 4420.
[23] D. Côte, I. A. Vitkin, *Opt. Express* **2005**, *13*, 148.
[24] S. L. Jacques, L. Wang, *Optical-Thermal Response of Laser-Irradiated Tissue*, Vol. 47, Springer, Boston, MA **1995**, p. 73.
[25] A. Major, R. Cisek, V. Barzda, *Opt. Express* **2006**, *14*, 12163.
[26] R. W. Boyd, *Nonlinear Optics* 3rd edittion, Academic Press, Burlington **2015**, 38.
[27] M. Samim, S. Krouglov, D. F. James, V. Barzda, *J. Opt. Soc. Am. B* **2016**, *33*, 2617.
[28] Y. Shi, W. M. McClain, R. A. Harris, *Phys. Rev. A* **1994**, *49*, 1999.
[29] F. Jaillon, H. Saint-Jalmes, *Appl. Optics* **2003**, *42*, 3290.
[30] V. Periyasamy, M. Pramanik, *J. Biomed. Opt.* **2014**, *19*, 45003.
[31] L. L. Carter, E. D. Cashwell, *Particle Transport Simulation with the Monte Carlo method*, Office of Public Affairs, U.S. Energy Research and Development Administration, Technical Information Center, Oak Ridge, TN **1975**.
[32] S. Alali, M. Ahmad, A. Kim, N. Vurgun, M. F. G. Wood, I. A. Vitkin, *J. Biomed. Opt.* **2012**, *17*, 45004.
[33] D. H. Goldstein, *Polarized Light*, CRC Press, Boca Raton, Florida, US, **2010**.
[34] J. Rička, M. Frenz, in *Optical-Thermal Response of Laser-Irradiated Tissue* (Eds: A. J. Welch, M. J. C. Van Gemert), Springer Netherlands, Dordrecht **2011**, p. 248.
[35] P. J. Campagnola, L. M. Loew, *Nat. Biotechnol.* **2003**, *21*, 1356.
[36] L. Barabesi, *Statistica Applicata* **1995**, *7*, 417.
[37] J. N. Gannaway, C. J. R. Sheppard, *Opt. Quantum Electron.* **1978**, *10*, 435.
[38] M. F. G. Wood, X. Guo, I. A. Vitkin, *J. Biomed. Opt.* **2007**, *12*, 14029.
[39] Y. Takano, M. Tanaka, *Appl. Optics* **1980**, *19*, 2781.
[40] J. Mertz, *C. R. Acad. Sci. Ser. IV* **2001**, *2*, 1153
[41] J. Mertz, L. Moreaux, *Opt. Commun.* **2001**, *196*, 325.
[42] M. F. G. Wood, N. Vurgun, M. A. Wallenburg, and I. A. Vitkin, *Phys. Med. Biol.*, **2011**,*56*, N115.
[43] P. A. Bautista, Y. Yagi, *J. Biomed. Opt.* **2012**, *17*, 56013.
[44] V. V. Tuchin, in: *Advances in Biophotonics* (Eds: B.C. Wilson, V. V. Tuchin, and S. Tanev), IOS Press, Amsterdam, Netherlands **2000**, pp. 85.
[45] D. J. Maitland, J. T. Walsh, *Lasers Surg. Med.* **1997**, *20*, 310.
[46] A. N. Bashkatov, E. A. Genina, V. I. Kochubey, V. V. Tuchin, *Proceedings of SPIE Volume 4162, Controlling Tissue Optical Properties: Applications in Clinical Study*, SPIE, Amsterdam, the Netherlands **2000**, p. 265.
[47] A. N. Bashkatov, E. A. Genina, V. I. Kochubey, V. V. Tuchin, *J. Phys. D Appl. Phys.* **2005**, *38*, 2543.
[48] S. van der Walt, S. C. Colbert, G. Varoquaux, *Comput. Sci. Eng.* **2011**, *13*, 22.
[49] J. D. Hunter, *Comput. Sci. Eng.* **2007**, *9*, 90.
[50] O. Nadiarnykh, P. J. Campagnola, *Opt. Express* **2009**, *17*, 5794.
[51] M. G. Monaghan, S. Kroll, S. Y. Brucker, K. Schenke-Layland, *Tissue Eng. Part C Methods* **2016**, *22*, 517.
[52] A. Tuer, D. Tokarz, N. Prent, R. Cisek, J. Alam, J. D. Dumont, L. Bakueva, J. Rowlands, V. Barzda, *J. Biomed. Opt.* **2010**, *15*, 26018.
[53] M. Samim, L. Kontenis, S. Krouglov, B. C. Wilson, V. Barzda, *Opt. Life Sci. Congr.* **2017** NTu3C.4. https://doi.org/10.1364/NTM.2017.NTu3C.4

SUPPORTING INFORMATION

Additional supporting information may be found online in the Supporting Information section at the end of the article.
Appendix S1 Supporting Information

How to cite this article: Fung KLB, Samim M, Gribble A, Barzda V, Vitkin IA. Monte Carlo simulation of polarization-sensitive second-harmonic generation and propagation in biological tissue. *J. Biophotonics*. 2018;e201800036. https://doi.org/10.1002/jbio.201800036

Supporting Information

Monte Carlo simulation of polarization-sensitive second-harmonic generation and propagation in biological tissue

K. L. Barry Fung, Masood Samim[*]*, Adam Gribble, Virginijus Barzda, and I. Alex Vitkin*

1. Pauli and Gell-Mann Matrices

The Pauli matrices are given as follows:

$$\tau_0 = \begin{bmatrix} 1 & 0 \\ 0 & 1 \end{bmatrix} \quad \tau_1 = \begin{bmatrix} -1 & 0 \\ 0 & 1 \end{bmatrix}$$
$$\tau_2 = \begin{bmatrix} 0 & 1 \\ 1 & 0 \end{bmatrix} \quad \tau_3 = \begin{bmatrix} 0 & i \\ -i & 0 \end{bmatrix} \tag{S1}$$

The Gell-Mann matrices are given as follows:

$$\lambda_1 = \sqrt{\frac{2}{3}}\begin{bmatrix} 1 & 0 & 0 \\ 0 & 1 & 0 \\ 0 & 0 & 1 \end{bmatrix} \quad \lambda_2 = \sqrt{\frac{1}{3}}\begin{bmatrix} 1 & 0 & 0 \\ 0 & 1 & 0 \\ 0 & 0 & -2 \end{bmatrix} \quad \lambda_2 = \begin{bmatrix} 1 & 0 & 0 \\ 0 & -1 & 0 \\ 0 & 0 & 0 \end{bmatrix}$$
$$\lambda_4 = \begin{bmatrix} 0 & 1 & 0 \\ 1 & 0 & 0 \\ 0 & 0 & 0 \end{bmatrix} \quad \lambda_5 = \begin{bmatrix} 0 & 0 & 0 \\ 0 & 0 & 1 \\ 0 & 1 & 0 \end{bmatrix} \quad \lambda_6 = \begin{bmatrix} 0 & 0 & 1 \\ 0 & 0 & 0 \\ 1 & 0 & 0 \end{bmatrix} \tag{S2}$$
$$\lambda_7 = \begin{bmatrix} 0 & -i & 0 \\ i & 0 & 0 \\ 0 & 0 & 0 \end{bmatrix} \quad \lambda_8 = \begin{bmatrix} 0 & 0 & 0 \\ 0 & 0 & -i \\ 0 & i & 0 \end{bmatrix} \quad \lambda_9 = \begin{bmatrix} 0 & 0 & -i \\ 0 & 0 & 0 \\ i & 0 & 0 \end{bmatrix}$$

2. Manipulation of Frames of Reference for Scattering

Two sets of rotations need to be performed for scattering: rotation of polarization with respect to the original direction of propagation, and the rotation of the direction of propagation. In both cases, the formulation follows Côte et al's initial implementation [1], and is briefly summarized here for completeness. The polarization of a photon propagating in the direction $\hat{e}_{prop}$ is described by a Stokes vector S defined according to two orthonormal axes, $\hat{e}_{\perp}$ and $\hat{e}_{\parallel}$. To rotate around the direction of propagation without changing S, a change of basis is needed. The new S', defined by axes $\hat{e}'_{\perp}$ and $\hat{e}'_{\parallel}$, is given by:

$$\hat{e}'_{\perp} = BR_{prop}(\phi)[1,0,0]^T \tag{S3}$$

$$\hat{e}'_{\parallel} = BR_{prop}(\phi)[0,1,0]^T \tag{$S4$}$$

$$S' = R_S(\phi)S \tag{$S5$}$$

The rotation matrix $R_{prop}(\phi)$ defines the rotation around the propagation direction:

$$R_{prop}(\phi) = \begin{bmatrix} \cos\phi & -\sin\phi & 0 \\ \sin\phi & \cos\phi & 0 \\ 0 & 0 & 1 \end{bmatrix} \tag{$S6$}$$

The matrix $R_S(\phi)$ that transforms the Stokes vector coordinates is:

$$R_S(\phi) = \begin{bmatrix} 1 & 0 & 0 & 0 \\ 0 & \cos 2\phi & \sin 2\phi & 0 \\ 0 & -\sin 2\phi & \cos 2\phi & 0 \\ 0 & 0 & 0 & 1 \end{bmatrix} \tag{$S7$}$$

Since all vectors are expressed in the lab coordinates $(\hat{x}, \hat{y}, \hat{z})$, the basis change matrix B:

$$B = \begin{bmatrix} \hat{e}_{\perp} \cdot \hat{x} & \hat{e}_{\parallel} \cdot \hat{x} & \hat{e}_{prop} \cdot \hat{x} \\ \hat{e}_{\perp} \cdot \hat{y} & \hat{e}_{\parallel} \cdot \hat{y} & \hat{e}_{prop} \cdot \hat{y} \\ \hat{e}_{\perp} \cdot \hat{z} & \hat{e}_{\parallel} \cdot \hat{z} & \hat{e}_{prop} \cdot \hat{z} \end{bmatrix} \tag{$S8$}$$

Once a vector has been rotated to the appropriate frame of reference, the direction and Stokes vector of the packet is altered via Equations (S9) – (S11), according to its deflection angle θ:

$$\hat{e}'_{\parallel} = BR_{\perp}(\theta)[0,1,0]^T \tag{S9}$$

$$\hat{e}'_{prop} = BR_{\perp}(\theta)[0,0,1]^T \tag{S10}$$

$$S_{out} = M_S(\theta)S' \tag{S11}$$

Where the rotation matrix $R_{\perp}(\theta)$ is given as:

$$R_{\perp}(\theta) = \begin{bmatrix} 1 & 0 & 0 \\ 0 & \cos\theta & -\sin\theta \\ 0 & \sin\theta & \cos\theta \end{bmatrix} \tag{S12}$$

and $M_S(\theta)$ is the Mueller scattering matrix as defined by Mie theory.

3. Input Stokes vectors for double Stokes-Mueller polarimetry measurements

The 9 incident polarizations used to probe the second order susceptibility of the material in simulation and experiment are: horizontal, vertical, diagonal, anti-diagonal, right circular, left circular, 22.5° linear polarization, right elliptical, and left elliptical. These polarizations are chosen as they are sufficiently different to provide a well-posed determination of the double Mueller Matrix or susceptibility correlation matrix $X^{(2)}$ – as seen in the thorough coverage these polarization states occupy on the Poincare sphere representation [2,3]

Expressed as Stokes vectors, the double Stokes-Mueller polarimetry measurement is represented via the following 4x9 matrix, with each column representing a single input state s_ω:

$$\begin{array}{c} [s_H \quad s_V \quad s_D \quad s_B \quad s_R \quad s_L \quad s_{22.5} \quad s_{RE} \quad s_{LE}] \\ = \begin{bmatrix} 1 & 1 & 1 & 1 & 1 & 1 & 1 & 1 & 1 \\ 1 & -1 & 0 & 0 & 0 & 0 & \sqrt{0.5} & -\sqrt{0.5} & 0 \\ 0 & 0 & 1 & -1 & 0 & 0 & \sqrt{0.5} & 0 & \sqrt{0.5} \\ 0 & 0 & 0 & 0 & 1 & -1 & 0 & \sqrt{0.5} & \sqrt{0.5} \end{bmatrix} \end{array} \quad \text{(S13)}$$

4. Sample Parameters

The measured sample thickness and angle parameters for each experiment are summarized in Table S1.

Table S1: Experimental sample parameters for increasing ω thickness beyond the focal point (Figure 3 experiment) and increasing 2ω thickness above the focal point (Figure 4 experiment). θ represents the bulk sample angle for the collagen fibres, relative to the vertical axis in the imaging plane, determined through analysis of the measured susceptibility correlation matrix $X^{(2)}$ and verified visually from SHG intensity images. The angle is used to represent the birefringence axis in the MC simulations, as well as to centre the von Mises distribution of fibre angle for SHG.

Experiment 1	**Thickness (µm)**	**Experiment 1**	**Thickness (µm)**	**θ (rads)**
For $\chi^{(2)}_{zzz}/\chi^{(2)}_{zxx}$	5 ± 2	For $\chi^{(2)}_{zzz}/\chi^{(2)}_{zxx}$ and *DOP*	8 ± 2	0.10 ± 0.14
	10 ± 2		12 ± 2	0.23 ± 0.12
	20 ± 2		16 ± 2	0.21 ± 0.05
	28 ± 2		20 ± 2	0.15 ± 0.04
	35 ± 2			
Experiment 2	**Thickness (µm)**	**θ (rads)**		
For $\chi^{(2)}_{zzz}/\chi^{(2)}_{zxx}$ and *DOP*	7 ± 2	0.77 ± 0.17		
	18 ± 2	0.79 ± 0.02		
	24 ± 2	0.74 ± 0.05		
	32 ± 2	0.72 ± 0.09		
	34 ± 2	0.71 ± 0.07		

References

1. D. Côte, and I.A. Vitkin, *Opt. Express*, **2005**, *13*, 148.

2. A. Gribble, D. Layden, and I. A. Vitkin *Opt. Letters*, **2013**, *13*, 5272

3. Y. Shi, W. M. McClain and R. A. Harris, *Phys. Rev. A*, **1994**, *49*, 1999.